PHYSICAL REVIEW FLUIDS **3**, 074702 (2018)

Coherent structures in a screen cylinder wake

Azlin Mohd Azmi,[1] Tongming Zhou,[2,*] Yu Zhou,[3] Hanfeng Wang,[4] and Liang Cheng[2]
[1]*Faculty of Mechanical Engineering, Universiti Teknologi MARA, 40450 Shah Alam, Selangor, Malaysia*
[2]*Department of Civil, Environmental and Mining Engineering, The University of Western Australia,*
35 Stirling Highway, Crawley, WA 6009, Australia
[3]*Institute for Turbulence-Noise-Vibration Interaction and Control, Shen Zhen Graduate School,*
Harbin Institute of Technology, People's Republic of China
[4]*School of Civil Engineering and Architecture, Central South University,*
Changsha, People's Republic of China

(Received 23 March 2018; published 13 July 2018)

Experiments were conducted in a wind tunnel to examine the development of coherent structures in a screen cylinder wake over a streamwise range of $10 \leqslant x/d \leqslant 60$ (where d is the diameter of the cylinder) at a Reynolds number Re of 7000. The screen cylinder was made of a stainless-steel wire mesh with a porosity (open area ratio) of 67%. Results showed that the flow can be classified into two distinct regimes, characterized by the averaged contributions from the coherent motion to the Reynolds stresses where vortices changed from growing to decaying. The first regime exhibited the growth of small-scale Kelvin-Helmholtz vortices in the shear layer through vortex merging. These small-scale vortices matured quite a distance downstream to form the "large-scale" coherent structures, marked by the change of the root-mean-square transverse velocity fluctuations from a twin-peak to a single peak profile, significantly extending the vortex formation length. The second regime was manifested by the slow decay of the fully formed large-scale vortices, designated by the weak vorticity exchange across the wake centerline. Conceptual models of the vortex formation and decay processes as well as the momentum transport in the screen cylinder wake were proposed and illustrated, and comparisons were made with that of a solid cylinder wake.

DOI: 10.1103/PhysRevFluids.3.074702

I. INTRODUCTION

Fluid flow past a circular cylinder has been studied extensively due to its significance in engineering applications. It is well established that this kind of flow is characterized by vortex shedding phenomena when the Reynolds number Re ($=U_\infty d/\nu$), where d is the diameter of the cylinder, U_∞ is the free stream velocity, and υ is the kinematic viscosity of the fluid, exceeds a critical value. As the vortices are shed regularly and alternatively from the cylinder, pressure distribution on the surface of the cylinder varies, resulting in periodic variation in the force components. If a cylinder is flexibly mounted and the frequency of shed vortices approaches its natural frequency, vibration of large amplitude will occur, which leads to the lock-in phenomenon. This vibration is generally termed vortex-induced vibrations (VIV).

VIV can be suppressed by increasing structural damping, avoiding resonance, streamlining a body, and applying an add-on device [1]. Shroud is one of the add-on devices effective in suppressing VIV [2]. Screen gauze is one of the shroud geometries used in addition to a perforated circular hole,

---

[*] Author to whom all correspondence should be addressed: tongming.zhou@uwa.edu.au

axial slat, and axial rod. An experiment conducted by Zdravkovich and Volk [3] showed that the highest reduction in the amplitude of vibration was achieved by the shroud made of a fine-mesh gauze in comparison to the square-holed and the circular-holed gauze (all of 36% porosity). The gauze shroud also affected the static pressure distribution more significantly than the other shrouds, for which there was a drastic change in the pressure distribution over the rear portion of the cylinder (between 80° and 160°). Recent studies revealed that screen gauze shrouds can suppress VIV from a circular cylinder by about 50–95% depending on the screen porosity and the inner-to-outer diameter gap ratio [4–6].

Classical studies on the characteristics of flow through screen gauzes can be found from the review of Laws and Livesey [7]. In addition to flow characteristics, there are also studies on the wake behind screen bodies. Miyata [8] reported that the flow behind fine screen gauze was governed by the instability process of the shear layer between the potential region and the very small turbulence region. Antonia *et al.* [9] speculated that the flow over a screen cylinder might not be dominated by the evolution of vortices in the mixing layers, a feature that uniquely characterized the flow in the screen strip wake [10–12]. Gansel *et al.* [13] showed that the wake characteristics behind various screen cylinders changed toward that of a solid cylinder at a porosity just below 75%. Levy *et al.* [14] argued that the surface porosity is not the key parameter in defining the flow topology of a porous screen, rather it is a nondimensional parameter based on the twine thickness, mesh void, and cylinder diameter that collapsed most of their experimental data. In a flow visualization test, Azmi and Zhou [15] demonstrated that, apart from porosity, the diameter ratio between the wire mesh and the shroud has a profound impact on the wake of a shrouded cylinder, with weaker vortex strength and longer formation length found for larger values of the nondimensional parameter.

However, most of the studies reviewed above were conducted in the near wake ($x/d < 5-10$), which might have been too small to examine the full development of the large-scale organized structures. In addition, the wake characteristics of this suppression device is largely unexplored. The present work is motivated by the need for additional insight into the development of the coherent structures. The primary aim is to investigate the formation, evolution, and characteristics of coherent structures in a screen cylinder wake. Results are compared with wakes generated by a solid cylinder and a screen strip. A conceptual wake model, illustrating the formation process and the momentum transport behavior, is also proposed. The statistical analyses and preliminary results of the screen cylinder wake have been reported earlier and can be found from [16,17].

II. EXPERIMENTAL DETAILS

The experiments were conducted in a blower-type wind tunnel with a test section of 380 mm (width) ×255 mm (height) and 1.8 m (length). The free stream velocity was uniform to 0.2% and the longitudinal turbulence intensity was less than 0.5%. A solid cylinder and a screen cylinder were used in the experiment. The diameter, d, of the solid cylinder and that of the screen cylinder were 10.1 and 21 mm, respectively. The solid cylinder was made of polished aluminum. The screen cylinder was made of a stainless-steel wire mesh of hole size a of 2 mm and a wire diameter d_w of 0.45 mm (Fig. 1). The porosity of the screen mesh β, defined as the ratio between the opening area to the total area, i.e., $a^2/(a+d_w)^2$, was 67%. Prior to making the screen cylinder, a width of 66 mm (i.e., πd) was marked on a screen mesh, which was then enfolded into a cylindrical form. The mesh was then cut through the middle of the aperture along the wire (i.e., along the cylinder axial direction, no wire was cut across except those aligned perpendicular to the axial direction). The two edges of the screen cylinder were then tied off using a 0.16-mm-diam wire every 3–4 cm along the cylinder axial direction. Due to the small diameter of the wire, the tie will be too small to affect the flow apparently. The diameter of the cylinder was uniform along the axial direction (with a tolerance of ±1%). It was monitored during the tests that there was no apparent deformation. Preliminary experiments conducted with the joint line orientated at 0° and 180° from the cylinder trailing edge gave similar results in the mean and root-mean-square values of the velocities (with a scatter less than 1%), causing the effect of the joint

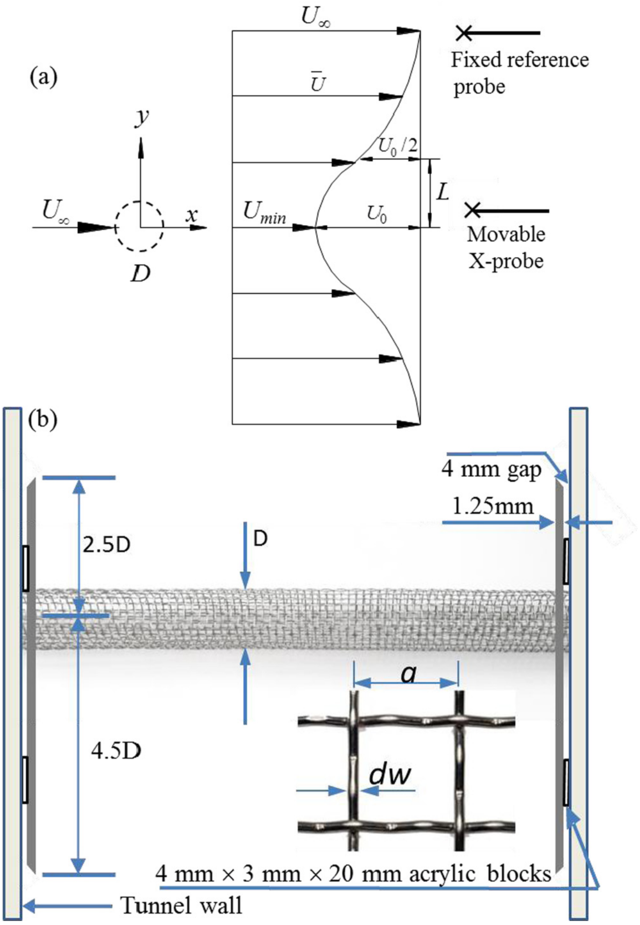

FIG. 1. Coordinate system, wake profile, and probe arrangement (a) and the top view of the arrangement of the screen cylinder (b). Note that the figures are not drawn to scale.

orientation to be negligible. All measurements were performed at Re $= 7000$, corresponding to a free stream velocity U_∞ of 10.4 and 5 m/s for the solid and screen cylinders, respectively. Following a suggestion by Stansby [18], end plates with dimensions $7d \times 7d$ were used. The cylinder models were fixed $2.5d$ from the leading edge of the end plates. The thickness of the plates was 1.25 mm with the leading and trailing edges being sharpened at an angle of 45°. They were fixed at about 4 mm from the tunnel side walls to keep them above the boundary layer. Measurements in the wake were conducted over a streamwise distance of $x/d = 10$–60 with an increment of 5. A hot-wire X probe was moved across the wake in the y direction to measure the longitudinal and transverse velocity components, u and v, respectively. Another X probe was fixed at the wake edge and at the same streamwise location as the first one to provide a phase reference to the measured velocity signals for phase-averaged analysis.

The hot wires were etched to a sensor length of 1 mm from Wollaston (Pt-10% Rh) wires with a wire diameter of 5 μm, which is long enough to neglect the heat loss at the ends of the sensors. The hot wires were operated with in-house constant temperature circuits at an overheat ratio of 1.5. Angle calibration was performed over ±20°. The effective angles of the inclined wires in the two X probes were 34°, 31°, 37°, and 43°. The output signals from the anemometers were low-pass

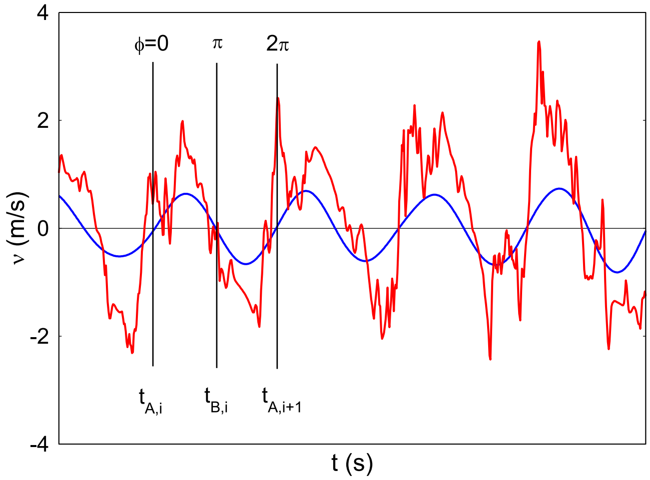

FIG. 2. Examples of the measured (red) and filtered (blue) velocity signals obtained at $x^* = 10$ and $y^* \approx 0.5$ in the solid cylinder wake.

filtered at a cutoff frequency f_c of 5200 Hz. The filtered signals were sampled at a frequency f_s of 10 400 Hz into a PC using a 16-bit A/D converter (National Instrument). The sampling period T_s was 30 s. Experimental uncertainties were inferred from the estimated inaccuracies in hot-wire calibration data as well as the scatter observed in repeating the experiments a number of times. The uncertainty for the time-average velocity $\bar{U}$ was estimated to be about ±2% while for the fluctuating velocities u and v the uncertainties of their rms values were about ±5% and ±6%, respectively. The uncertainty for Reynolds shear stress $\langle uv \rangle$ was about 8%, where the angular brackets denote time averaging.

III. PHASE AND STRUCTURAL AVERAGING

According to Hussain and Reynolds [19], a turbulent signal B can be decomposed into a mean value, $\bar{B}$, and a fluctuation component β. The fluctuation component can be decomposed further into a coherent component $\tilde{\beta}$ and the remainder component β_r, i.e.,

$$B = \bar{B} + \beta = \bar{B} + (\tilde{\beta} + \beta_r). \tag{1}$$

Identification of the coherent structures at a given frequency can be done through the phase-average method. To use the phase-averaging analysis, the v-signal measured by the reference X probe was band-pass-filtered with the central frequency set at the peak frequency identified on the energy spectra. A fourth-order Butterworth filter was used. The filtered signal was then used to condition the v-signal measured by the movable probe. Examples of the measured and filtered velocity signals are given in Fig. 2. The two phases of particular interest are identified on the filtered signal v_f, viz.,

$$\text{Phase } A: \quad v_f = 0 \ \text{ for } \ \frac{dv_f}{dt} > 0, \tag{2}$$

$$\text{Phase } B: \quad v_f = 0 \ \text{ for } \ \frac{dv_f}{dt} < 0. \tag{3}$$

These two phases correspond to time $t_{A,i}$ and $t_{B,i}$ (measured from an arbitrary time origin), respectively. The phase ϕ, calculated between the time $t_{A,i}$ and $t_{B,i}$, corresponds to the longitudinal distance in terms of the average vortex wavelength λ, viz.,

$$\phi = \pi \frac{t - t_{A,i}}{t_{B,i} - t_{A,i}}, \quad t_{A,i} \leqslant t \leqslant t_{B,i}, \tag{4}$$

$$\phi = \pi \frac{t - t_{B,i}}{t_{A,i+1} - t_{B,i}} + \pi, \quad t_{B,i} < t \leqslant t_{A,i+1}. \tag{5}$$

The interval between phases A and B is transformed so that $t_{B,i} - t_{A,i} = 0.5/f_s$. This interval is further divided into 30 subintervals. The difference between the local phase at each y location of the movable probe and the reference phase of the fixed X probe is used to produce the phase-averaged sectional streamlines and contours of the coherent quantities in the (ϕ, y) plane. The phase-average of an instantaneous quantity B can be calculated by

$$\langle B \rangle_k = \frac{1}{N} \sum_{i=1}^{N} B_{k,i}, \tag{6}$$

where B can be any quantities such as velocity or vorticity, N (>1200) is the number of vortex shedding for each measurement, and k represents the considered phase. The phase-averaged Reynolds shear stress $\tilde{u}\tilde{v}$ can also be calculated viz.

$$\langle \beta\gamma \rangle = \tilde{\beta}\tilde{\gamma} + \langle \beta_r \gamma_r \rangle, \tag{7}$$

where β and γ can each either be u or v.

The transport characteristics of the vortical structures can be described by structural averaging of a quantity. After extracting the coherent component of the desired quantities, the velocities, for example, the coherent and incoherent contributions to Reynolds stresses can be obtained in terms of the structural average. The structural average (denoted by a double overbar) is defined by

$$\overline{\overline{\tilde{\beta}\tilde{\gamma}}} = \frac{1}{k_1 + k_2 + 1} \sum_{-k_1}^{k_2} \tilde{\beta}\tilde{\gamma}, \tag{8}$$

where $k_1 = k_2 = 30$ is equal to the number of intervals for phase-averaging. Detailed descriptions of the phase and structural averaging can be found in Ref. [20].

IV. RESULTS AND DISCUSSION

A. Mean velocity, Reynolds stresses, and spectra

The distributions of the time-average velocity $\bar{U}$ in the streamwise direction, in the format of velocity deficits in the wake, are presented in Fig. 3. Hereafter, the superscript asterisk denotes normalization by the free stream velocity and/or the cylinder diameter. The distributions appear generally symmetrical about the centerline $y^* = 0$. The profiles for the solid cylinder [Fig. 3(a)] agree quite well with those shown in Ref. [21] validating the present measurement. The maximum velocity deficit U_0^*, as shown by the peak value, decreases as x^* increases. The mean velocity profiles in the screen cylinder wake [Fig. 3(b)] reveal a much larger velocity deficit for $x^* \leqslant 30$. The velocity gradients in the shear layers over this region are considerably larger than that at other wake locations, associated with the shear layer development. For $x^* > 30$, the values of U_0^* are comparable to that in the solid cylinder wake, and the velocity profiles become slightly flatter in the central region.

The distributions of the root-mean-square (rms) values of the longitudinal velocity and the transverse velocity, u' and v', respectively, are given in Figs. 4 and 5, where a superscript prime denotes rms values. The profiles of u'/U_∞ in the solid cylinder wake [Fig. 4(a)] are symmetric about $y^* = 0$ and reveal a twin-peak behavior at $x^* = 10$, consistent with that shown by Zhou *et al.* [22]. The magnitude of u' decays in the streamwise direction. The twin-peak profile is distinctly evident in

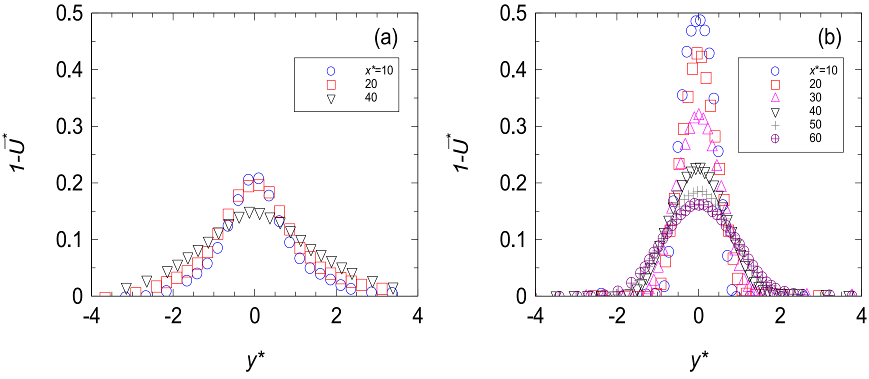

FIG. 3. Normalized mean velocity distributions in the wake of (a) solid cylinder and (b) screen cylinder at different downstream locations. The maximum velocity deficit U_0^* occurs at $y^* = 0$.

the screen cylinder wake [Fig. 4(b)]. The rms values increase gradually from the centerline ($y^* = 0$) to the highest in the shear layers, reflecting the intensifying activities within the shear region.

The differences in the distributions of v'/U_∞ in both wakes are obvious (Fig. 5). The v'/U_∞ values in the solid cylinder wake [Fig. 5(a)] are maxima on the centerline of the wake, and they decrease monotonically toward the edge of the wake, indicating a signature of a vortex street. At the centerline, the maximum value of v'/U_∞ decreases with downstream distance due to the decay of the vortex structures. In contrast to the solid body wake, the v'/U_∞ distributions in the screen cylinder wake [Fig. 5(b)] can be clearly divided into two regions. For $x^* \leqslant 20$, the twin peak is evident where there is a gradual increase of rms value in the wake, from the lowest value at the centerline to the maximum in the shear layers ($y^* \approx 0.55$). As x^* increases, the peaks become wider, indicating the growth of the shear layer. For $x^* \geqslant 30$, the v'/U_∞ values have a plateau in the central part of the wake, indicating that the two shear layers merge at the wake centerline, interacting to form a single vortex street, similar to that in the solid cylinder wake. The highest plateau is evident at $x^* = 40$, and it decreases slowly thereafter. However, the plateaus are much lower in magnitude than that in the solid cylinder wake, signifying weak vortex intensity in the screen cylinder wake. This will be discussed later from the phase-averaged flow pattern in Sec. IV B.

Figure 6 shows spectra ϕ_v obtained in the two-cylinder wakes at different downstream locations, where the frequency corresponding to the peaks on the spectrum is defined as the Strouhal number St,

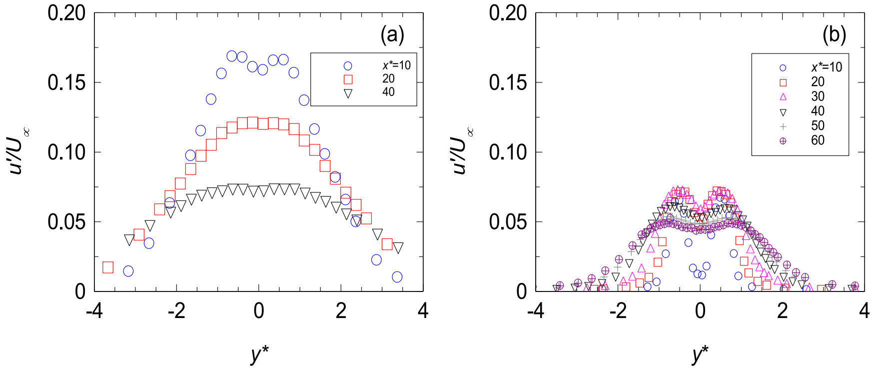

FIG. 4. Normalized distributions of the rms longitudinal velocity in the wake of (a) solid cylinder and (b) screen cylinder.

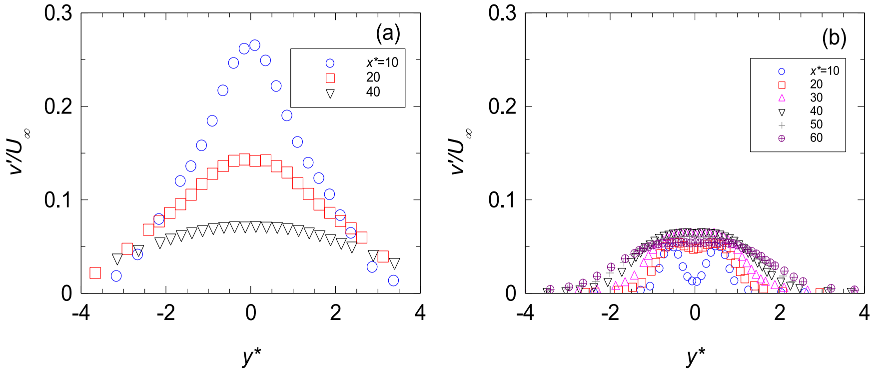

FIG. 5. Normalized distributions of the rms transverse velocity in the wake of (a) solid cylinder and (b) screen cylinder.

i.e., St (or f^*) $= f_0 d/U_\infty$, and f_0 is the vortex shedding frequency. For easy viewing of Fig. 6, each spectrum is shifted downward by one order of magnitude relative to the spectrum at the previous location. Figure 6(a) clearly shows a sharp peak at $x^* = 10$ at a single frequency f_0 of 201 Hz**,** which corresponds to $f^* = 0.2$ signifying an apparent vortex shedding for the solid cylinder wake. The peak frequency f_0 remains the same (as indicated by the red arrow in the figure) although the peak height reduces with x^*, signifying the decay of vortices in the streamwise direction. On the contrary, there is a weak broadband peak in the energy spectra of the screen cylinder wake [Fig. 6(b)] at $x^* = 10$, attributed to the roll-up vortices in the shear layers, which marks the dissimilarity in the near-wake behavior of both cylinders. At $x^* = 20$, a broadband peak at $f^* = 0.26$ appears, slightly sharper than that at $x^* = 10$, signifying the emergence of some periodicity of the organized fluid structures in the wake. At $x^* = 30$, the peak at $f^* = 0.23$ is obvious, designating the formation of the large-scale structures. The broadband peak is still noticeable further downstream with a trend of slightly decreasing frequency, as indicated by the inclined line in the figure. For example, the peak frequency decreases from 0.23 at $x^* = 30$ to 0.202 at $x^* = 60$.

Spectra along the outer edge in the screen cylinder wake [Fig. 6(c)] show the existence of periodicity throughout the wake where noticeable broadband peaks are apparent at all measured locations, even at $x^* = 10$, albeit at much higher frequency than other downstream locations. Huang and Keffer [11] described the same behavior for their screen strip wake ($\beta = 40\%$ and $\mathrm{Re} = 1.1 \times 10^4$) and attributed the broad peak at $x^* = 1$ to the Kelvin-Helmholtz instability of vortex sheets generated at the mesh edge, which then roll up into discrete vortices, comparable to the single shear layer development. They also observed that as x^* increases from 10 to 30, the periodicity becomes obvious and the peak magnitude becomes larger. This trend, i.e., the growth of the peak and decrease of the broad peak location toward lower frequencies along the streamwise direction, signifies the growth of the vortical structures within the shear layers, although this growth is not significant from $x^* = 30$ for our screen cylinder. For the screen cylinder wake, this behavior could be due to an increase in the average wavelength, assuming it is slowly increasing in convective velocity, implying an amalgamation of vortices has taken place, which is responsible for the formation of the large-scale structures in the screen cylinder wake, similar to the findings of Huang and Keffer [11] and Antonia and Mi [12]. The continuous decrease of the peak frequency shows that the merging process does not occur at a fixed downstream location. Fascinatingly, the shifting of the broad peak to lower frequencies resembles that of a solid cylinder far wake discussed by Browne *et al.* [23]. Their v spectra showed clear evidence of a broad "secondary" peak near the shedding frequency that decreases in the streamwise direction, where this peak is associated with the secondary organized motion, which is prominent in the self-preserving far wake. This additional finding may suggest that the same mechanism is responsible for the formation of the organized motion in both wakes, which would need to be corroborated in the future.

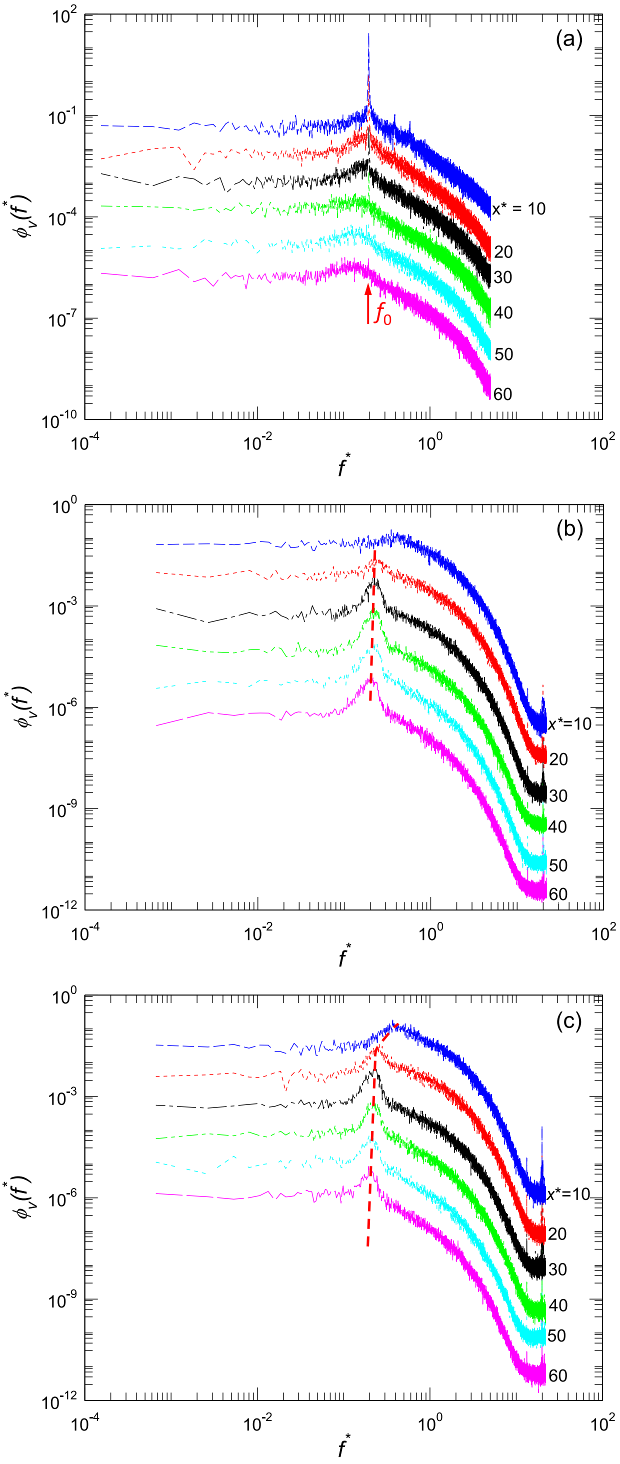

FIG. 6. Energy spectra $\phi_v(f^*)$ in the wake of (a) solid cylinder and (b) screen cylinder measured at $y^* = 0.5$ and (c) screen cylinder measured at the wake edge. The red dashed lines in (b) and (c) indicate the change of the peak frequency with x^*.

TABLE I. Characteristic properties of vortices in the wake of the solid cylinder and the screen cylinder. The values in the brackets are from Zhou and Antonia [10].

			Solid cylinder			
x/d	y_c/d	U_c/U_∞	fd/U_∞	$\varphi_{uv}(f)$	$\tilde{\omega}^*_{z\max}$	α
10	0.30	0.83	0.20	−94	1.0	45°
20	0.50 [0.50]	0.85 [0.87]	0.20 [0.21]	−92 [−94]	0.4	37°
40	0.60	0.87	0.20	−86	0.12	26
			Screen cylinder			
x/d	y_c/d	U_c/U_∞	fd/U_∞	$\varphi_{uv}(f)$	$\tilde{\omega}^*_{Z\max}$	α
10	0.80	0.76	0.380	−171	0.80	10.0°
20	0.70 [0.70]	0.79 [0.78]	0.260 [0.280]	−170 [−169]	0.50	15.0°
30	0.70	0.81	0.230	−160	0.35	21.5°
40	0.8	0.82	0.223	−160	0.25	33.0°
50	0.80	0.87	0.210	−170	0.20	33.0°
60	1.00	0.90	0.202	−170	0.15	33.0°

B. Phase-averaged coherent vorticity field and sectional streamlines

After the coherent signals $\tilde{u}$ and $\tilde{v}$ have been detected, the phase-averaged vorticity $\tilde{\omega}_z$ is calculated via

$$\tilde{\omega}_z = \frac{\partial(\bar{V}+\tilde{v})}{\partial x} - \frac{\partial(\bar{U}+\tilde{u})}{\partial y} \approx \frac{\Delta\tilde{v}}{\Delta x} - \frac{\Delta(\bar{U}+\tilde{u})}{\Delta y}. \tag{9}$$

The separation in the streamwise direction, Δx, can be obtained using Taylor's hypothesis, i.e., $\Delta x = -U_c\Delta t = -U_c/f_s$. The average convection velocity U_c of the vortices is given by the velocity $\bar{U}+\tilde{u}$ at the vortex center identified by the location of the maximum phase-averaged vorticity $\tilde{\omega}_{\max}$. The separation in the y direction, Δy, is the distance between two adjacent measurement locations of the probe across the wake.

Table I lists some of the characteristic properties of the vortices for both wakes, including the location of the vortex center y_c, the average convection velocity U_c, and the phase shift between velocity signals u and v, $\varphi_{uv}(f)$. The phase shift at the vortex shedding frequency between velocity signals u and v is given by $\varphi_{uv}(f) = \tan^{-1}[Q_{uv}/C_{uv}]$, where Q_{uv} is the quadrature spectrum and C_{uv} is the cospectrum of u and v. The experimental errors in y_c and U_c at $x/d = 10$ are about 3%. The errors are expected to be bigger further downstream due to increased uncertainty in determining the vortex center. Results from Zhou and Antonia [10] on the wakes of a solid cylinder and a screen strip of 50% porosity at $x/d = 20$ and $\mathrm{Re} = 5600$ are also included in the brackets. The U_c/U_∞ value increases with x/d in the solid cylinder wake. This trend agrees well with that reported by Zhou and Antonia [24]. The same trend is found for U_c in the screen cylinder wake. In addition, the difference of vortices between different wakes can also be quantified in terms of the phase shift. The phase-shift values for the solid cylinder wake agree reasonably well with that of [10], indicative of the alternating periodic vortex shedding in the form of Kármán vortices. For the screen cylinder wake, the phase-shift values are 160°–170° at all measurement locations, which agrees very well at $x/d = 20$ (169°) with that of a screen strip reported by [10].

Figures 7 and 8 show the isocontours of the phased-averaged vorticity of the solid cylinder and the screen cylinder wakes, respectively. Hereafter, all negative contours are shown by dashed lines, and positive contours are shown by solid lines. Due to the regular shedding of the vortices in the wakes, one shedding period that corresponds to a phase angle from 0 to 2π can be calculated. About 2000 periods of data were obtained over the measurement duration of 30 s at each y location. One period

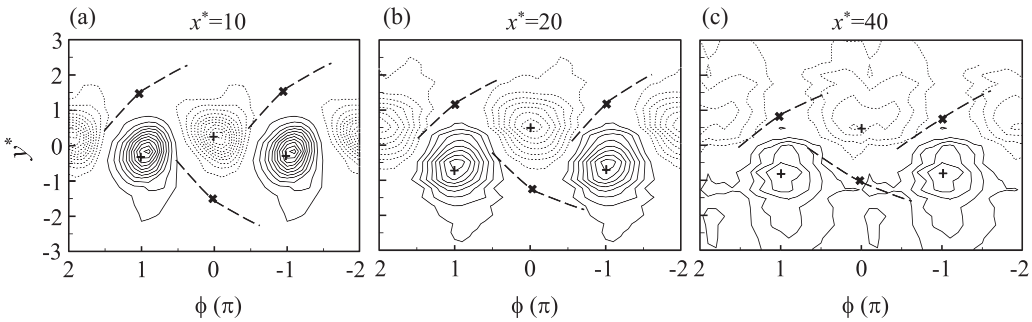

FIG. 7. Phase-averaged coherent spanwise vorticity, $\tilde{\omega}_z^*$, for the solid cylinder wake at (a) $x^* = 10$ (minimum contour value -1.0, maximum contour value 1.1, contour interval 0.1), (b) $x^* = 20$ (-0.35,0.4,0.05), and (c) $x^* = 40$ (-0.12,0.12,0.03). Vortex centers and saddles are marked by a plus and a cross, respectively. The thick dashed lines represent the diverging separatrices that pass through the saddles.

is divided into 30 phases, ϕ, and the measured data are then averaged at a given phase over the 2000 periods. The phase-averaged contours are also plotted over the phase angle -2π to 0 by mirroring those from 0 to 2π for clearer pictures of the flow structures. The phase ranging from -2π to $+2\pi$ can be inferred in terms of a streamwise distance, and $\phi = 2\pi$ corresponds to the vortex wavelength $\lambda(=U_c/f_o)$. The flow direction is from left to right.

There are profound differences in the shape, strength, and size of the vortices and their evolutions in the two wakes. Figure 7 clearly illustrates the large-scale vortical structures and their evolution in the streamwise direction. At $x^* = 10$, the $\tilde{\omega}_z^*$ contours display the well-known Kármán vortex street with a maximum concentration of 1.1 occurring at $y^* \cong 0.3$, consistent with that reported by [22]. A staggered pattern is evident where the positive and negative vortices penetrate the other side of the

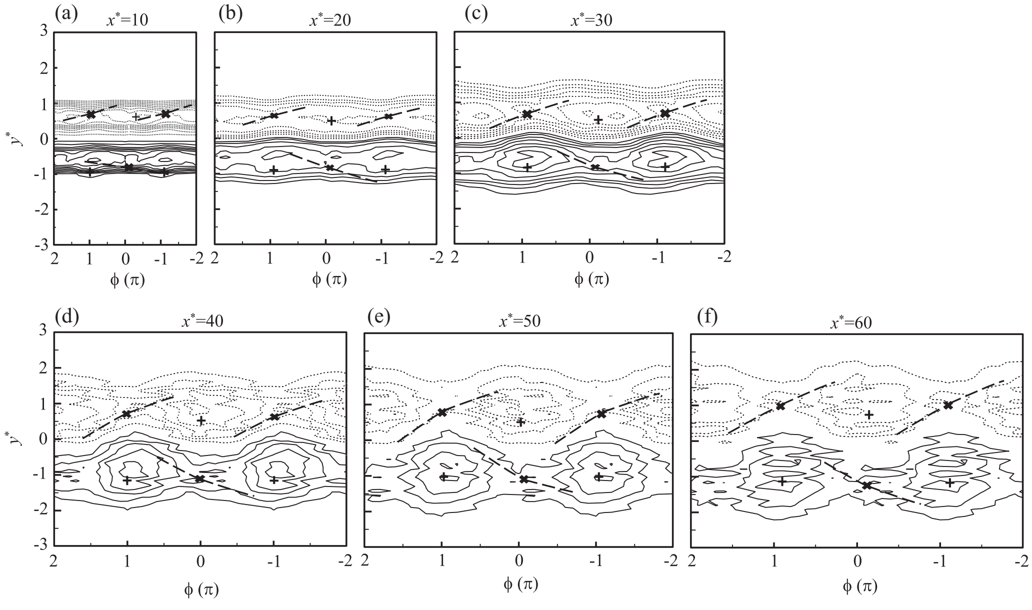

FIG. 8. Phase-averaged coherent vorticity, $\tilde{\omega}_z^*$, for the screen cylinder wake at (a) $x^* = 10$ (-0.8,0.8,0.1); (b) $x^* = 20$ (-0.5,0.5,0.1); (c) $x^* = 30$ (-0.35,0.35,0.05); (d) $x^* = 40$ (-0.25,0.25,0.05); (e) $x^* = 50$ (-0.2,0.2,0.05); and (f) $x^* = 60$ (-0.15,0.15,0.05). Vortex centers and saddles are marked by a plus and a cross, respectively. The thick dashed lines represent the diverging separatrices that pass through the saddles.

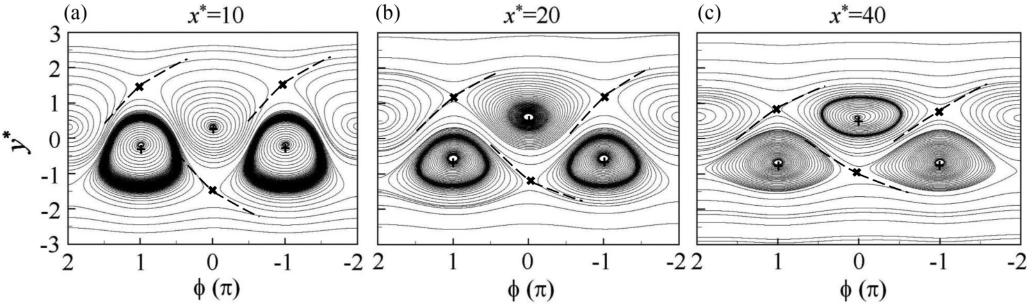

FIG. 9. Phase-averaged sectional streamlines for the solid cylinder wake at (a) $x^* = 10$; (b) 20; and (c) 40. Vortex centers and saddles are marked by a plus and a cross, respectively. The thick dashed lines represent the diverging separatrices that pass through the saddles.

wake. At $x^* = 20$, there is a similar vortex structure with a lower maximum concentration of 0.4. At $x^* = 40$, the maximum concentration decreases to 0.12, signifying an apparent reduction in vortex strength with x^*. For the screen cylinder wake (Fig. 8), the $\tilde{\omega}_z^*$ contours display small-scale vortices in the shear layers separated by an undisturbed core layer at the central region when $x^* < 20$. This undisturbed core layer should be due to the permeable effect of the screen cylinder. At $x^* \approx 20$, the core layer starts to undulate, implying that the interaction between the opposite signed vortices has started to take place. At $x^* = 30$, groups of vorticities are distributed in the vicinity of the vortex cores around the phase of $\phi = 0$, suggesting an amalgamation process when evolving downstream. As a result, the spanwise vorticity contours become more apparent than those closer to the cylinder. Vortices still mature subsequently until $x^* = 40$, where the large-scale structures can be seen to be fully developed with larger lateral spacing than that at $x^* = 30$. In view of the coherent vorticity contours for $x^* \geqslant 40$, the lateral and streamwise spacings of the vortices do not vary much. In addition, the maximum vorticity concentration decays by about 20% from $x^* = 40$ to 50 and by 25% from $x^* = 50$ to 60 in the screen cylinder wake, while a decay of 64% is noticeable from $x^* = 10$ to 20 in the solid cylinder wake, signifying a sluggish decay in the former. Due to these behaviors, it is conjectured that the vortical structures in the screen cylinder wake will persist an extended distance downstream. The vorticity contours also show a small amount of vorticity enveloping the vortex cores on each side of the wake, which is also observed in a screen strip wake [25], a distinct feature from that of the solid cylinder wake. However, the vorticity envelope in the screen strip wake was absent, and the periodicity was less noticeable at $x^* = 50$ and 100, corroborating the persistence of structures in the screen cylinder wake.

The phase-averaged sectional streamlines of the two wakes are shown in Figs. 9 and 10, respectively. The solid cylinder wake (Fig. 9) is consistent with that of the vorticity contours in Fig. 7. For the screen cylinder wake (Fig. 10), small-scale elliptical structures are evident in the shear layers at $x^* = 10$ and 20, consistent with the vorticity contours in Fig. 8. The size of these structures increases when evolving downstream. There is a core layer at the central region separating the two shear layers, which is not disturbed especially at $x^* = 10$. At $x^* = 20$, the size of the vortices is large enough to cause the core layer to undulate slightly. The undulation of this layer becomes more apparent further downstream due to the increase of the vortices. Evidently, the lateral spacing between saddle points or vortex centers is different in the two wakes. For example, the spacing between foci is approximately 0.55, 1.1, and 1.2 for $x^* = 10$, 20, and 40, respectively, in the solid cylinder wake. The corresponding foci spacing is relatively large (1.5, 1.45, 1.4, 1.7, 1.6, and 1.8 at $x^* = 10$, 20, 30, 40, 50, and 60, respectively) in the screen cylinder wake. In addition, the diverging separatrices in the solid cylinder wake can extend across the wake centerline, which indicates the riblike structures connecting the counter-rotating vortices on the opposite sides. This is in contrast

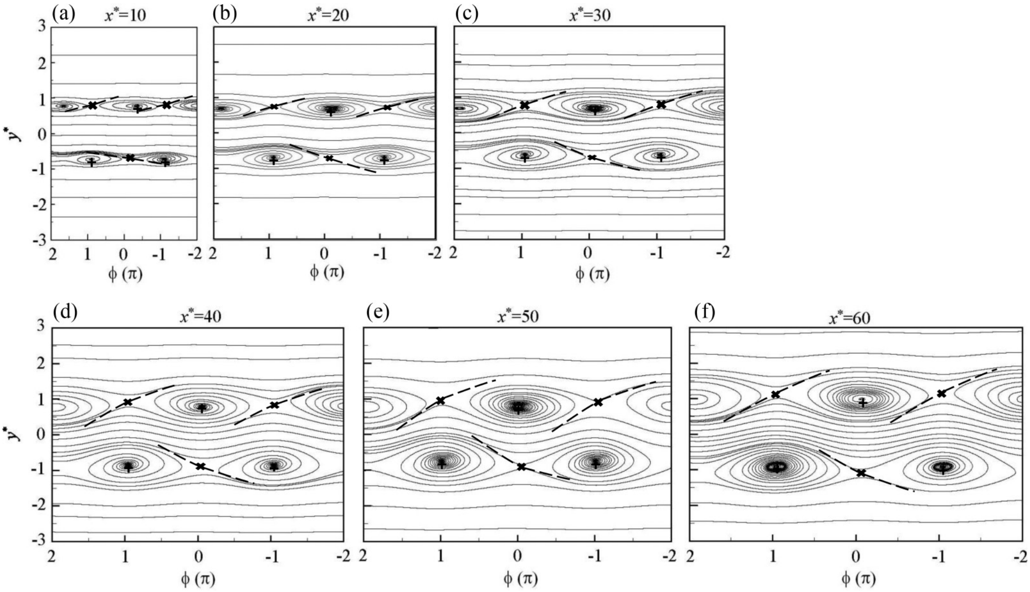

FIG. 10. Phase-averaged sectional streamlines for the screen cylinder wake at (a) $x^* = 10$; (b) 20; (c) 30; (d) 40; (e) 50; and (f) 60. Vortex centers and saddles are marked by a plus and a cross, respectively. The thick dashed lines represent the diverging separatrices that pass through the saddles.

to that in the screen cylinder wake, where the separatrices are elongated in the streamwise direction between the same rotating vortices.

C. Vorticity transport

It has been mentioned that the interaction of vortical structures across the centerline in the screen cylinder wake starts at $x^* = 20$ and a slow decay of the fully formed vortices is observed after $x^* = 40$. To understand the interaction between vortices and the vorticity decay in the two wakes, the effective turbulent vorticity flux density vector, $\boldsymbol{J}$, as introduced by Kolar *et al.* [26] is examined. The vector provides a measure for the vorticity transport and is defined by $\boldsymbol{J} = \{J^x, J^y\}$, where

$$J^x = \frac{\partial}{\partial y}\left[\frac{\langle v_r^2\rangle - \langle u_r^2\rangle}{2}\right] + \frac{\partial}{\partial x} u_r v_r, \tag{10}$$

$$J^y = \frac{\partial}{\partial x}\left[\frac{\langle v_r^2\rangle - \langle u_r^2\rangle}{2}\right] - \frac{\partial}{\partial y} u_r v_r. \tag{11}$$

Figures 11 and 12 show the effective vorticity flux density vectors $\tilde{J}^*$ at different streamwise locations. $\tilde{J}^*$ is directed from higher to lower coherent vorticity concentration, and its length indicates the strength of the flux density. The thick solid lines denote the outermost vorticity contours as seen in Figs. 7 and 8. The vector and the number on the upper left-hand side of the figure provide the correspondence between the vector length and the vorticity magnitude. In the solid cylinder wake (Fig. 11), at $x^* = 10$, the relatively long vectors are directed toward and cross the vortex borders, illustrating the strength of vorticity exchange and thus vorticity cancellation between the opposite-signed vortices, which is responsible for the fast decay of vortices, decaying by 64% from $x^* = 10$ to 20. At $x^* = 20$, the exchange of vorticity is less vigorous than that at $x^* = 10$ as indicated by the shorter vector length, but still apparent. At $x^* = 40$, the vectors are very weak and the interactions between the counter-rotating vortices disappear almost completely. In the screen cylinder

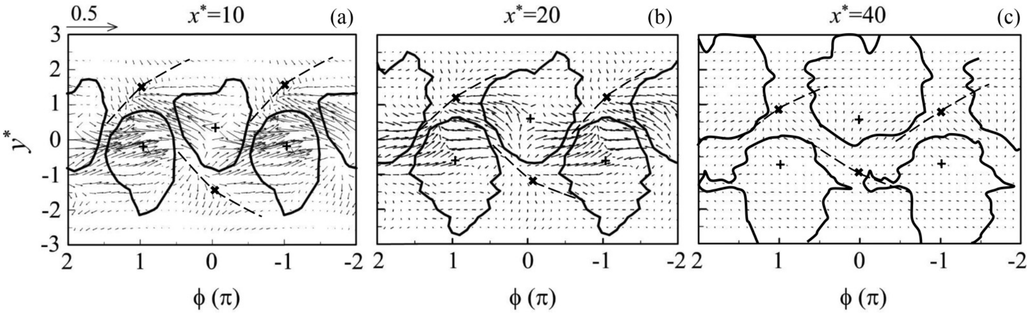

FIG. 11. Spanwise vorticity flux density vectors for the solid cylinder wake at (a) $x^* = 10$; (b) 20; and (c) 40. The solid lines represent the outermost of the vorticity contours. Vortex centers and saddles are marked by a plus and a cross, respectively. The thick dashed lines represent the diverging separatrices that pass through the saddles.

wake (Fig. 12), however, at $x^* = 10$, the vectors mostly concentrate in the vicinity of the outermost vorticity contours. There is no interaction between the upper and lower vortices. The interaction is evident at $x^* = 20$, where the relatively long vectors are directed toward and move across the centerline. These interactions are enhanced further downstream until $x^* = 40$. The long vectors tend to occur along and pointed toward the diverging separatrices, but they do not appear to interact strongly with those from the adjacent vortex, as observed in the solid cylinder wake. The crossing of the long vectors from one border to the adjacent vortex border is obvious from $x^* = 20$ to 40, but not so evident at $x^* \geqslant 50$, indicating a weak exchange of vorticity that results in a slow decay of the vorticity concentration.

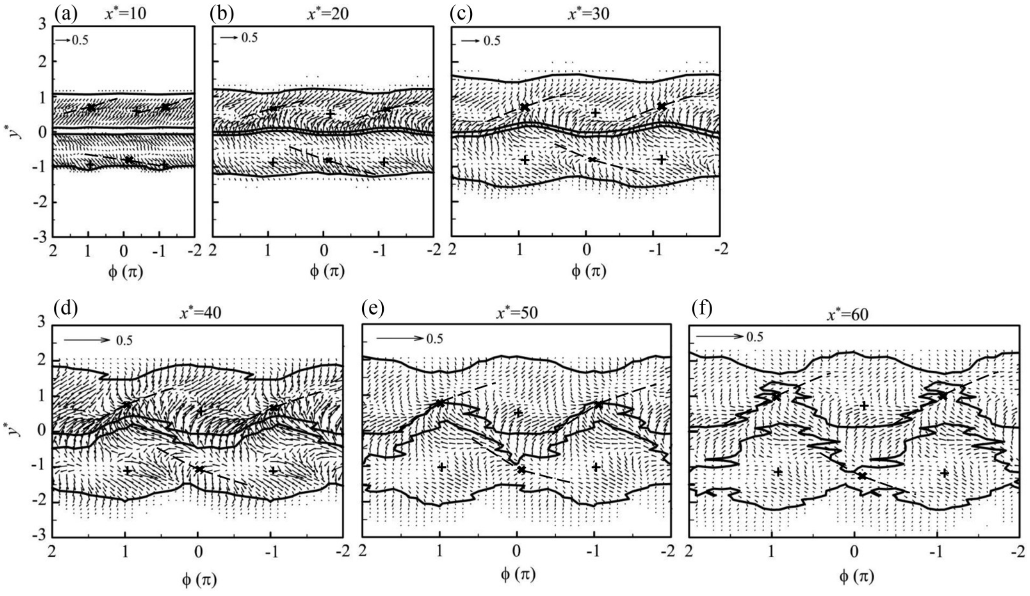

FIG. 12. Spanwise vorticity flux density vectors for the screen cylinder wake at (a) $x^* = 10$; (b) 20; (c) 30; (d) 40; (e) 50; and (f) 60. The solid lines represent the outermost of the vorticity contours. Vortex centers and saddles are marked by a plus and a cross, respectively. The thick dashed lines represent the diverging separatrices that pass through the saddles.

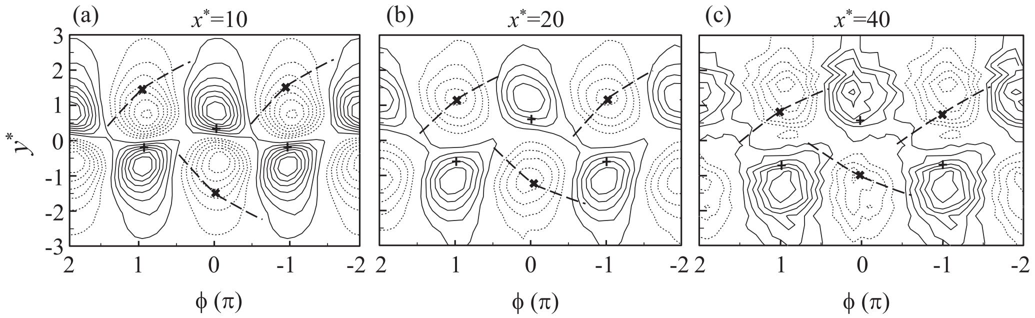

FIG. 13. Phase-averaged velocity, $\tilde{u}^*$, for the solid cylinder wake at (a) $x^* = 10$ (minimum contour value -0.14, maximum contour value 0.14, contour interval 0.02), (b) $x^* = 20$ (-0.04,0.05,0.01), and (c) $x^* = 40$ (-0.01,0.012,0.002). Vortex centers and saddles are marked by a plus and a cross, respectively. The thick dashed lines represent the diverging separatrices that pass through the saddles.

D. Coherent fluctuating velocities

The isocontours of the phase-averaged streamwise and lateral velocities ($\tilde{u}$ and $\tilde{v}$) are depicted in Figs. 13–16. In the solid cylinder wake, the $\tilde{u}^*$ contours display approximate up-down antisymmetry about the wake centerline (Fig. 13) while the $\tilde{v}^*$ contours display antisymmetry about $\phi = 0$ (Fig. 15), similar to those reported in Ref. [21]. A similar approximate antisymmetry of the $\tilde{u}^*$ and $\tilde{v}^*$ contours is also evident in the screen cylinder wake (Figs. 14 and 16), but there are significant differences between the two. For example, at $x^* = 10$, both the maximum concentrations of $\tilde{u}^*$ and $\tilde{v}^*$ in the solid cylinder wake are about more than 95% higher than that in the screen cylinder wake. In fact,

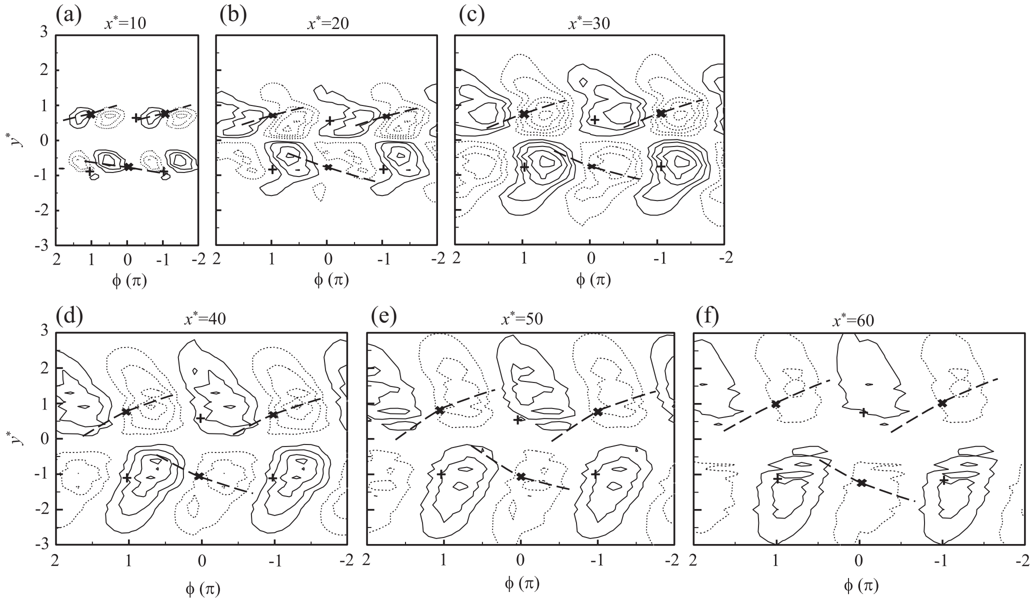

FIG. 14. Phase-averaged velocity, $\tilde{u}^*$, for the screen cylinder wake at (a) $x^* = 10$ (-0.015,0.015,0.005); (b) $x^* = 20$ (-0.02,0.02,0.005); (c) $x^* = 30$ (-0.025,0.025,0.005); (d) $x^* = 40$ (-0.02,0.02,0.005); (e) $x^* = 50$ (-0.01,0.015,0.005); and (f) $x^* = 60$ (-0.01,0.01,0.005). Vortex centers and saddles are marked by a plus and a cross, respectively. The thick dashed lines represent the diverging separatrices that pass through the saddles.

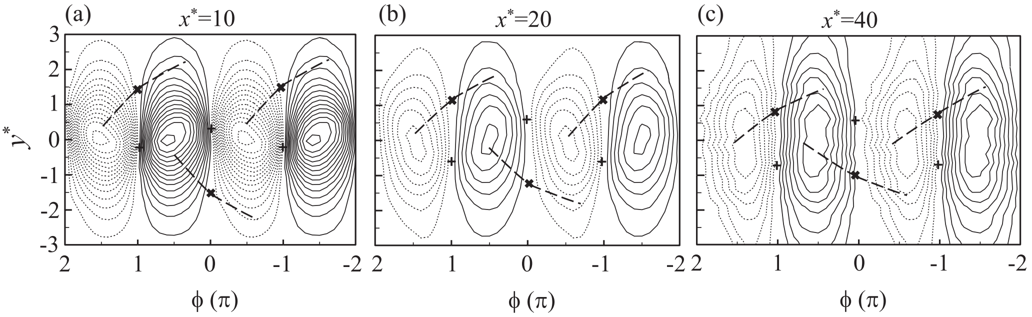

FIG. 15. Phase-averaged velocity, $\tilde{v}^*$, for the solid cylinder wake at (a) $x^* = 10$ (minimum contour value -0.28, maximum contour value 0.28, contour interval 0.02), (b) $x^* = 20$ (-0.12,0.12,0.02), and (c) $x^* = 40$ (-0.035,0.035,0.005). Vortex centers and saddles are marked by a plus and a cross, respectively. The thick dashed lines represent the diverging separatrices that pass through the saddles.

the concentration of the former is still about more than 60% higher than the latter at $x^* = 20$. In the solid cylinder wake, the maximum concentration decreases with downstream distance. In the screen cylinder wake, however, the $\tilde{u}^*$ and $\tilde{v}^*$ contours become more regular and apparent with x^* and the concentration increases until up to $x^* = 30$ and 40, respectively, before it decreases slightly thereafter. These results indicate the existence of two separate regimes in the screen cylinder wake. One is the developing regime where the small-scale structures are growing through vortex merging, and the other is the decaying regime where the large-scale vortices decay gradually. These two regimes are also evident from the Reynolds shear stress contours, which will be discussed in the next section.

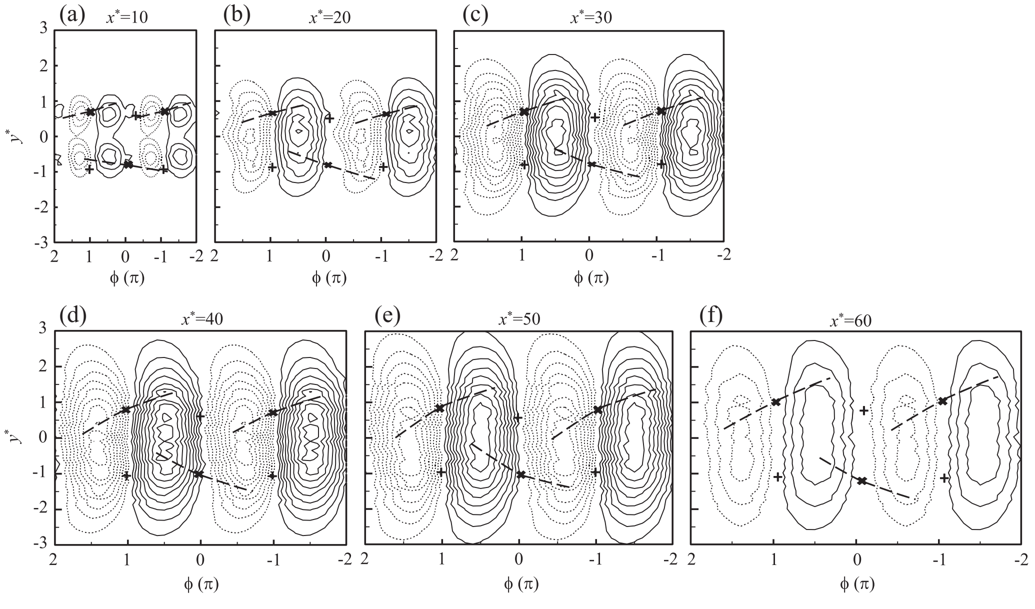

FIG. 16. Phase-averaged velocity, $\tilde{v}^*$, for the screen cylinder wake at (a) $x^* = 10$ (-0.015,0.015,0.005); (b) $x^* = 20$ (-0.025,0.03,0.005); (c) $x^* = 30$ (-0.04,0.04,0.005); (d) $x^* = 40$ (-0.04,0.045,0.005); (e) $x^* = 50$ (-0.035,0.04,0.005); and (f) $x^* = 60$ (-0.03,0.03,0.01). Vortex centers and saddles are marked by a plus and a cross, respectively. The thick dashed lines represent the diverging separatrices that pass through the saddles.

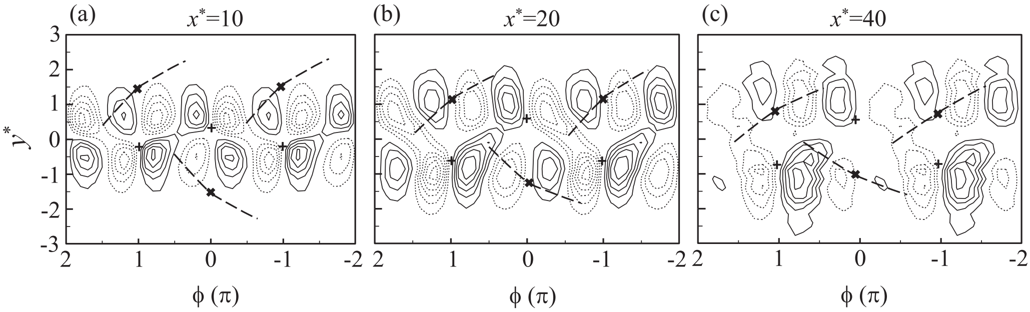

FIG. 17. Phase-averaged Reynolds shear stress, $\tilde{u}^*\tilde{v}^*$, for solid cylinder wake at (a) $x^* = 10$ (minimum contour value -0.02, maximum contour value 0.02, contour interval 0.004), (b) $x^* = 20$ $(-0.003,0.003,0.0005)$, and (c) $x^* = 40$ $(-0.00015,0.00023,0.00005)$. Vortex centers and saddles are marked by a plus and a cross, respectively. The thick dashed lines represent the diverging separatrices that pass through the saddles.

E. Coherent and incoherent Reynolds shear stress

The $\tilde{u}^*\tilde{v}^*$ contours in the solid cylinder wake at $x^* = 10$ and 20 (Fig. 17) display the well-established cloverleaf pattern about the vortex center as reported previously [20,27]. While the $\tilde{u}^*\tilde{v}^*$ contours in the solid cylinder wake show a near antisymmetry about both $\phi = 0$ and $y^* = 0$ (except at $x^* = 40$), the screen cylinder wake displays a near antisymmetry only about $y^* = 0$ (Fig. 18), where the negative $\tilde{u}^*\tilde{v}^*$ contours overwhelm the positive ones in the upper wake and the positive contours overwhelm the negative ones in the lower wake, reflecting a structural difference in the two wakes. The contours at the locations where the large-scale structures are evident ($x^* \geqslant 40$) show no

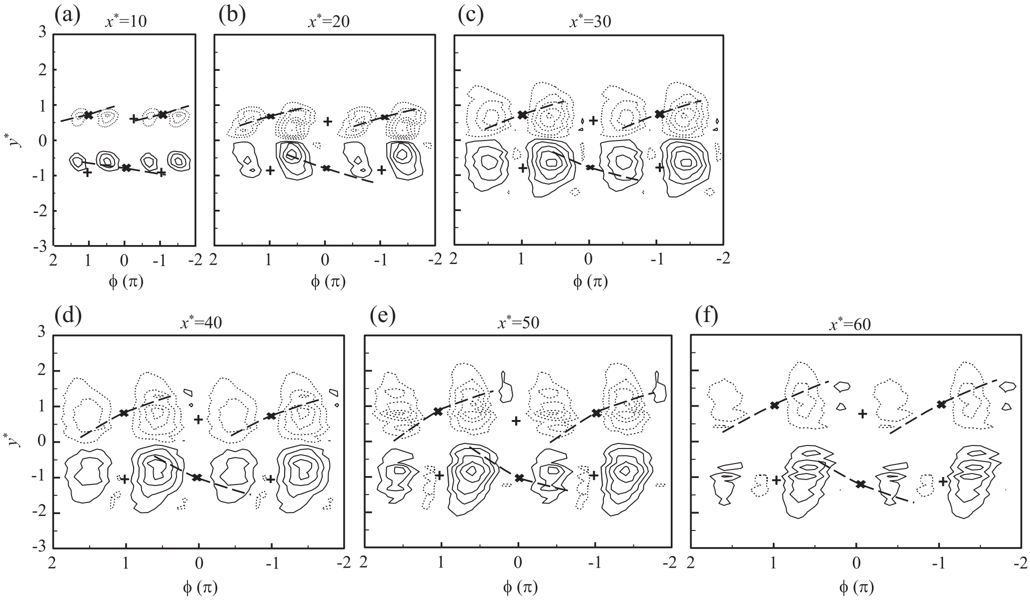

FIG. 18. Phase-averaged Reynolds shear stress, $\tilde{u}^*\tilde{v}^*$, for the screen cylinder wake at (a) $x^* = 10$ $(-0.0003,0.0003,0.0001)$; (b) $x^* = 20$ $(-0.005,0.004,0.0002)$; (c) $x^* = 30$ $(-0.0009,0.0009,0.0002)$; (d) $x^* = 40$ $(-0.0007,0.0007,0.0002)$; (e) $x^* = 50$ $(-0.0004,0.0005,0.0001)$; and (f) $x^* = 60$ $(-0.0002,0.0003,0.0001)$. Vortex centers and saddles are marked by a plus and a cross, respectively. The thick dashed lines represent the diverging separatrices that pass through the saddles.

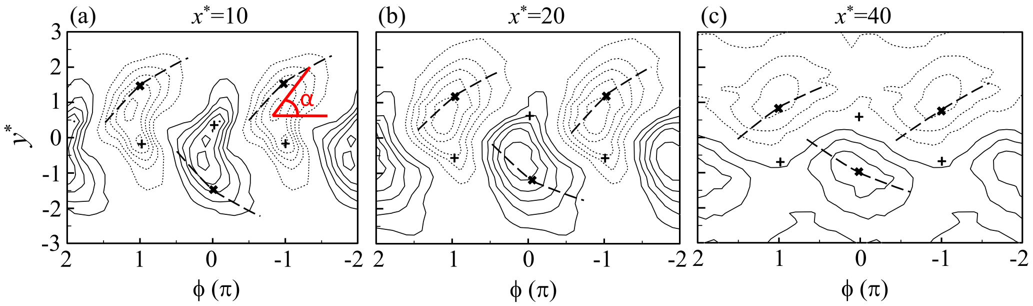

FIG. 19. Phase-averaged incoherent Reynolds shear stress, $\langle u_r^* v_r^* \rangle$, for the solid cylinder wake at (a) $x^* = 10$ $(-0.01, 0.01, \text{contour interval} = 0.002)$, (b) $x^* = 20$ $(-0.005, 0.005, 0.001)$, and (c) $x^* = 40$ $(-0.0015, 0.0015, 0.0005)$. The stretching angles α are given in Table II. Vortex centers and saddles are marked by a plus and a cross, respectively. The thick dashed lines represent the diverging separatrices that pass through the saddles.

regular cloverleaf pattern such as that of the solid cylinder wake that separates the vortices equally into four quadrants according to the sign of $\tilde{u}^*\tilde{v}^*$ (as illustrated in the vortex topology in Fig. 24). Interestingly, this transport of momentum is also different from that of [27], where the $\tilde{u}^*\tilde{v}^*$ contours of the screen strip wake resembled the clover-leaf pattern similar to that of the solid cylinder wake, but the size and the concentration of the negative contours were bigger than the positive contours. This asymmetry was exhibited in both the near wake ($x^* = 20$) and the far wake ($x^* = 220$) of the screen strip. Note also the marked increase of the $\tilde{u}^*\tilde{v}^*$ magnitude (about 160% increase) from $x^* = 10$ to 20.

In general, the contours of the incoherent Reynolds shear stress $\langle u_r^* v_r^* \rangle$ in the solid cylinder wake (Fig. 19) resemble those of [20] where they are stretched at an angle α along the diverging separatrix and the extrema are located mostly near the saddles ($x^* \geqslant 20$). The extrema of the $\langle u_r^* v_r^* \rangle$ contours at $x^* = 10$ tend to be near the foci. The angles α (Table I) decrease with x^* from 45° at $x^* = 10$ to just 26° at $x^* = 40$. The contours penetrate across the centerline to the opposite side. At $x^* = 40$, the negative and positive $\langle u_r^* v_r^* \rangle$ contours dominate the upper and lower wake, respectively, strikingly similar to the contours exhibited in the screen cylinder wake (Fig. 20), apparently due to the weak vortex strength and weak interaction across the wake centerline. The stretching angle α changes from 10° at $x^* = 10$ to 33° at $x^* = 40$ and remains constant thereafter. It is also obvious that the contours of $\tilde{u}^*\tilde{v}^*$ and $\langle u_r^* v_r^* \rangle$ in the screen cylinder wake are different qualitatively in the region $x^* = 10-30$ and $x^* = 40-60$, conforming the two flow regimes described in the previous section.

F. Coherent and incoherent contributions to Reynolds stresses

Figures 21 and 22 illustrate the results of the time-averaged values, coherent and incoherent contributions to the Reynolds stresses for both the solid cylinder and the screen cylinder wakes, respectively. The time-averaged distributions of the Reynolds stresses in the solid cylinder wake (Fig. 21) are either symmetrical ($\overline{u^{*2}}$ and $\overline{v^{*2}}$) or antisymmetric ($\overline{u^*v^*}$) about $y^* = 0$ at all locations. The distributions in the screen cylinder wake (Fig. 22) also exhibit symmetrical and antisymmetric behavior. Generally, the magnitudes of the velocity variances are much smaller in the screen cylinder wake than that in the solid cylinder wake, on the order of about 1/10. The coherent contributions to $\overline{u^{*2}}$ and $\overline{v^{*2}}$ of the solid cylinder wake at $x^* = 10$ are very significant, in contrast to their counterparts of the screen cylinder wake, which are almost negligible at this location. In fact, the major contribution to $\overline{v^{*2}}$ in the central region of the solid cylinder wake comes from the coherent motion, which is also true for $\overline{u^*v^*}$, indicating the strong coherent motion in the form of regular periodic vortex shedding in the near wake of the solid cylinder. The coherent motion depletes with downstream distance, and at $x^* = 40$ the coherent contributions are almost zero. For the screen cylinder wake, the incoherent motion largely amounts to $\overline{u^2}$, $\overline{v^{*2}}$ and $\overline{uv}$ at all locations. It is obvious that the coherent contribution

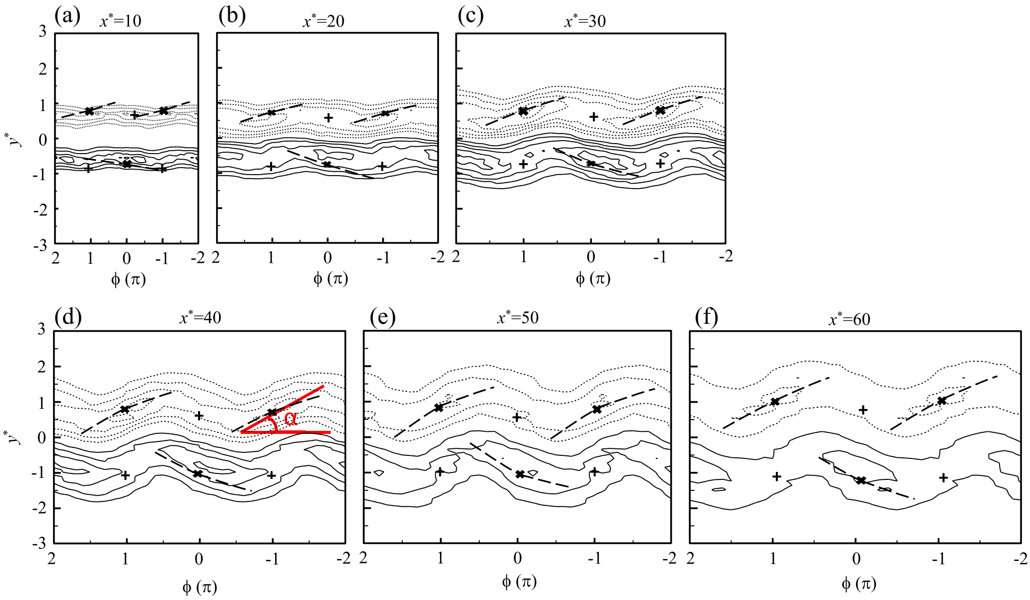

FIG. 20. Phase-averaged incoherent Reynolds shear stress, $\langle u_r^* v_r^* \rangle$, for the screen cylinder wake at (a) $x^* = 10$ (-0.002, 0.002, contour interval = 0.0005); (b) $x^* = 20$ (-0.002, 0.002, 0.0005); (c) $x^* = 30$ (-0.0025, 0.0025, 0.0005); (d) $x^* = 40$ (-0.002, 0.002, 0.0005); (e) $x^* = 50$ (-0.0015, 0.0015, 0.0005); and (f) $x^* = 60$ (-0.001, 0.001, 0.0005). The stretching angles α are given in Table II. Vortex centers and saddles are marked by a plus and a cross, respectively. The thick dashed lines represent the diverging separatrices that pass through the saddles.

to $\overline{v^{*2}}$ increases with x^* with the largest contribution occurring at $x^* = 40$, before it decays slowly thereafter. In contrast to the profiles of $\overline{\overline{\tilde{v}^*}}$ in the solid cylinder wake, which decay quickly, the decay of $\overline{\overline{\tilde{v}^*}}$ at $x^* \geqslant 40$ in the screen cylinder wake is much slower. The twin peak profile of $\overline{v^{*2}}$ in the screen cylinder wake for $x^* < 30$ is replaced by a single peak profile at $x^* \geqslant 30$. The twin peak should indicate the small-scale vortices in the shear layers, which are evident in the sectional streamlines (Fig. 10). This result suggests that in the screen cylinder wake, there exists a "critical" location where the large-scale structures have formed and grew in the streamwise direction before decaying slowly.

To quantify the coherent contribution to the Reynolds stresses, the dependence of the ratio $\overline{\overline{\tilde{\beta}\tilde{\gamma}}} \, / \, \overline{\beta\gamma}$ on x^* is examined. Since this ratio varies with y^*, the averaged contribution across the wake from the vortical structures is used, which is defined as

$$(\overline{\overline{\tilde{\beta}\tilde{\gamma}}}/\overline{\beta\gamma})_m = \int_{-\infty}^{\infty} |\overline{\overline{\tilde{\beta}\tilde{\gamma}}}| dy^* \Bigg/ \int_{-\infty}^{\infty} |\overline{\beta\gamma}| dy^* \, . \tag{12}$$

The results are listed in Table II. Generally, the averaged coherent contribution to $\overline{v^2}$ is greater than that to $\overline{u^2}$ in the solid cylinder wake. The coherent contributions to $\overline{u^2}$, $\overline{v^2}$, and $\overline{uv}$ in the solid cylinder wake at $x^* = 10$ are significant, much larger than that in the screen cylinder wake at the same location. This result indicates that the vortices generated in the former near-wake are much stronger than that in the latter. The larger contribution to $\overline{v^2}$ than to $\overline{u^2}$ is also depicted in the screen cylinder wake. While the values $(\overline{\overline{\tilde{\beta}\tilde{\gamma}}}/\overline{\beta\gamma})_m$ in the solid cylinder wake decrease with x^*, they show a different trend in the screen cylinder wake, i.e., $(\overline{\overline{\tilde{v}}} \, / \, \overline{v^2})_m$, $(\overline{\overline{\tilde{u}}} \, / \, \overline{u^2})_m$, and $(\overline{\overline{\tilde{u}\tilde{v}}} \, / \, \overline{uv})_m$ increases until $x^* = 40$ before decreasing slowly thereafter, consistent with the decaying regime described previously.

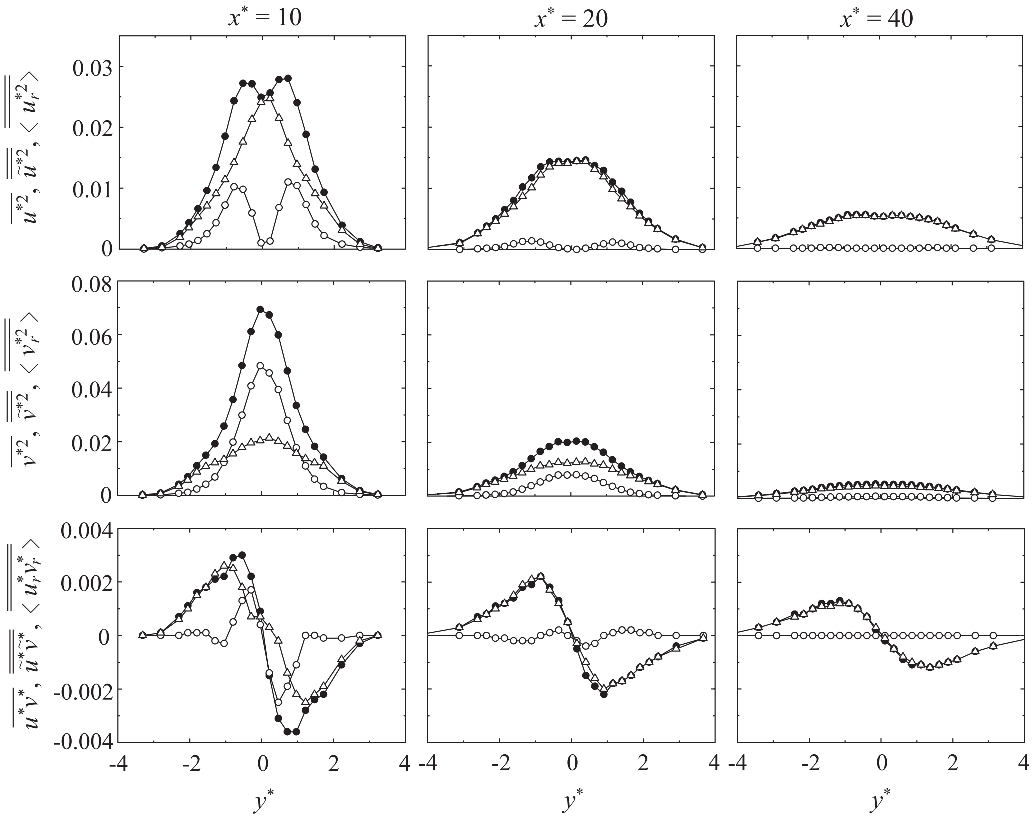

FIG. 21. Coherent (○) and incoherent (Δ) contributions to time-averaged (•) Reynolds stresses at different downstream locations for the solid cylinder wake.

G. Formation and decay in the cylinder wakes

Figure 23 shows the conceptual models of the vortex formation and decay processes in both wakes. In the present study, the Reynolds number Re is 7000, which is in the shear-layer transition regime

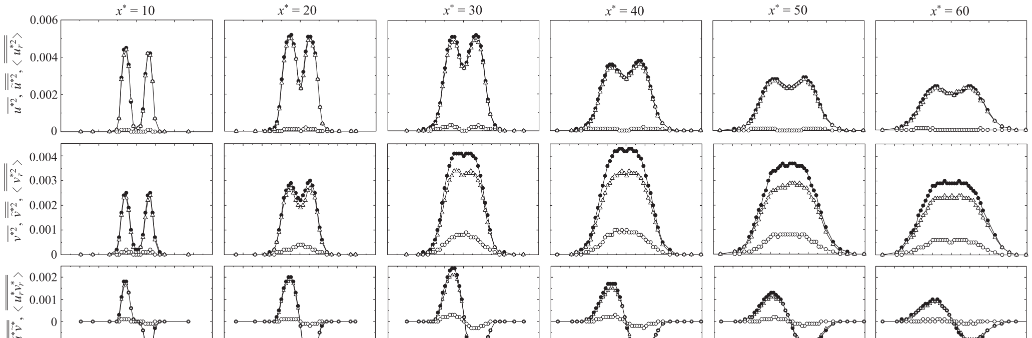

FIG. 22. Coherent (○) and incoherent (Δ) contributions to time-averaged (•) Reynolds stresses at different downstream locations for the screen cylinder wake.

TABLE II. Percentage of averaged contributions from the coherent motion to the Reynolds stresses in the wakes of the solid cylinder and the screen cylinder.

	Solid cylinder		
x/d	$(\overline{\overline{\tilde{u}^2}} \,/\, \overline{u^2})_m$	$(\overline{\overline{\tilde{v}^2}} \,/\, \overline{v^2})_m$	$(\overline{\overline{\tilde{u}\tilde{v}}} \,/\, \overline{uv})_m$
10	28.0	51.1	28.6
20	8.7	21.7	8.1
40	5.1	1.6	0.6
	Screen cylinder		
x/d	$(\overline{\overline{\tilde{u}^2}} \,/\, \overline{u^2})_m$	$(\overline{\overline{\tilde{v}^2}} \,/\, \overline{v^2})_m$	$(\overline{\overline{\tilde{u}\tilde{v}}} \,/\, \overline{uv})_m$
10	0.20	6.8	5.6
20	3.1	13.9	9.5
30	4.3	19.9	12.6
40	4.5	21.8	13.2
50	3.4	21.2	9.2
60	2.8	19.6	5.0

as classified by Williamson [28]. A crucial feature of the flow structure in a plain circular cylinder wake in this regime is the onset of the Kelvin-Helmholtz (KH) instability in the free shear layers formed a short distance from the surface of the cylinder before forming a vortex street. Once formed, the vortices decay quickly due to the interaction and stretching between the opposite signed vortices across the centerline, resulting in the vorticity cancellation as can be inferred from the present study [Fig. 23(a)]. In the screen cylinder wake [Fig. 23(b)], the small-scale vortices in the shear layers are generated at the mesh edge due to the KH instability. These shear layer vortices grow downstream through vortex pairing/merging, similar to that of a mixing layer [29]. In pairing, two adjacent vortices of the same rotation spin around each other, come closer, and then merge. Apart from the shed vortices on the scale of the mesh wire, there are also jets emerging from the screen pores. These vortices and jets would likely interact with each other and eventually diffuse, resembling a near-grid flow. It is believed that the combined effects of eddies and jets (or whichever is more dominant)

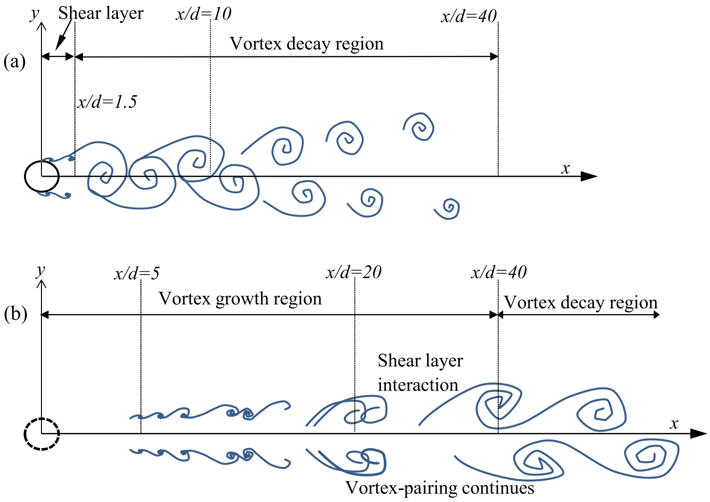

FIG. 23. Conceptual models of vortex formation and decay processes in wakes of (a) solid cylinder and (b) screen cylinder. Sketches are not drawn to scale.

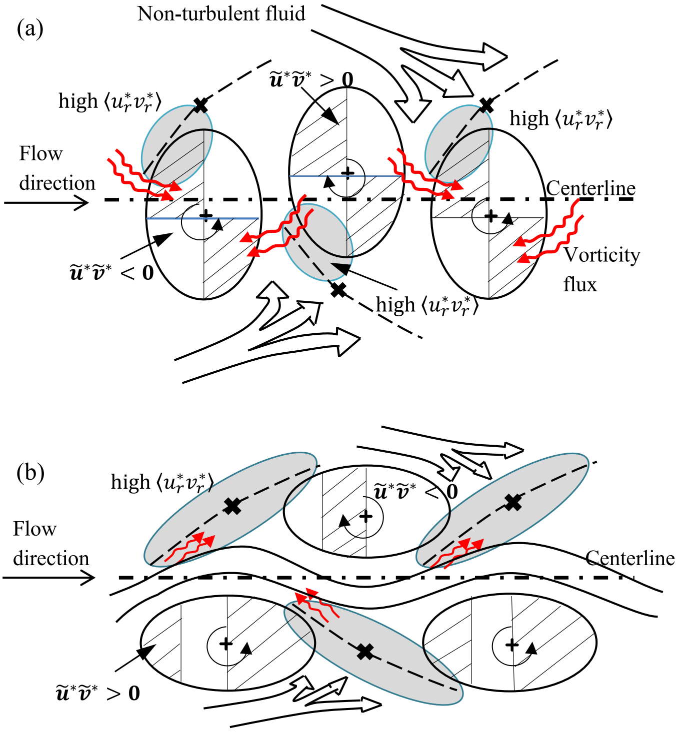

FIG. 24. Summary sketches of topology of (a) solid cylinder at $x/d = 10$ and (b) screen cylinder at $x/d = 40$. ▨: regions with positive $\tilde{u}^*\tilde{v}^*$; ▢ : regions of high $\langle u_r^* v_r^* \rangle$; ⤳ : vorticity flux; ≈ : undulated buffer layer. Vortex centers and saddles are marked by a plus and a cross, respectively. The thick dashed lines represent the diverging separatrices that pass through the saddles. The vortex center represents maximum coherent spanwise vorticity.

characterize the core region that prevents the shear layers from interacting and ultimately increases the formation length. At $x^* \approx 20$, the vortices in the shear layers may be large enough, causing the core region to undulate, resulting in the interactions between them across the wake centerline. The successive pairing process of the paired vortices in the shear layers continues until $x^* = 40$, where the vortices have completely formed. The vortex thereafter decays much slower than that in the solid cylinder wake, which is mainly due to the weak interaction between the opposite-signed vortices across the wake centerline.

The most salient features of the "large-scale" structures in the two wakes based on the phase-averaged contours are summarized in the topologies shown in Fig. 24 (i.e., at $x^* = 10$ and 40 for the solid cylinder and the screen cylinder wakes, respectively). First, the foci in the solid cylinder wake are closer to the centerline in contrast to its counterpart. Second, the outermost of the vorticity contours for the solid cylinder wake extends across the centerline, whereas those of the screen cylinder wake are separated by an undulated region around the centerline, indicating a weak interaction between the upper and the lower rows of vortices. Interestingly, the vortex structures in the screen cylinder wake are qualitatively similar to that in the solid cylinder far wake at $x^* = 420$ and $\mathrm{Re} = 1200$ [30], where the large-scale structures were elliptical in shape and oscillated on either side of the flow centerline and the critical points (foci and saddles) alternatingly located at $y^* \approx \pm 1$. Third, for both negative and positive vortices in the solid cylinder wake, the first and third quadrants yield $\tilde{u}^*\tilde{v}^* < 0$ while in the screen cylinder wake, the region of $\tilde{u}^*\tilde{v}^* < 0$ in the upper wake (or the region of $\tilde{u}^*\tilde{v}^* > 0$ in the lower wake) overwhelms the vortices, a totally contrasting behavior exhibited by the coherent motion in transporting momentum. The coherent motion within the vortices in the screen cylinder wake does not contribute strongly to the shear stress as it does in the solid cylinder wake, as reflected from $(\overline{\overline{\tilde{v}^2}} \;/\; \overline{v^2})_m$ in Table II; the incoherent motion plays a more dominant role in the transfer of momentum. Regions of significant shear stress associated with the incoherent motion are oriented mostly along the separatrices, as shown by the shaded areas in Fig. 24. Finally, while the vorticity flux mainly aligns along the diverging separatrix in the screen cylinder wake, that of the large magnitude crosses the borders of the oppositely signed vortices in the solid cylinder wake, resulting in a fast vortex decay process for the latter case.

V. CONCLUSIONS

The vortical structures in a screen cylinder (of 67% porosity) wake were experimentally studied at a Reynolds number of 7000 over a region $10 \leqslant x^* \leqslant 60$. The vortex formation, momentum transport, and their streamwise evolution were discussed, and a comparison with that of a solid cylinder wake was made. The main conclusions are summarized as follows:

(1) The differences in the structure of the vortices between the wakes of a solid cylinder and a screen cylinder were quantitatively reflected by the phase shift at the shedding frequency between u and v. The phase shift was about 90° in the near wake of the solid cylinder but about 160°–170° in the screen cylinder wake. The vortical structures in the screen cylinder wake alternated above and below the centerline and were separated by a core region, similar to that in the screen strip wake. Interestingly, these structures were also qualitatively similar to those of the solid cylinder far wake [30] with similar spectral behavior of the shifting of the broad peak toward lower frequencies with streamwise distance [23], surmising that the same mechanism could be responsible for the generation of the vortical structures in the two flows.

(2) The vortex formation region in the screen cylinder wake has been extended significantly, which should be due to the permeable effect of the cylinder that prevents the immediate interaction between the upper and lower shear layers. In the near wake, shear-layer vortices were formed as a result of the Kelvin-Helmholtz instability. At about $x^* \geqslant 20$, the vortices in the shear layers were sufficiently large so as to interact with each other across the centerline. These vortices amalgamated, grew in size, and decreased in frequency while evolving downstream and developed into the "large-scale" coherent structures that were fully formed at $x^* = 40$.

(3) After the complete growth of the large-scale structures, the decay rate of vortices in the screen cylinder wake was much slower than that in the solid cylinder wake. The vorticity transport displayed vigorous interactions of opposite-signed vortices across the centerline in the solid cylinder wake, which significantly sped up its decay. In contrast, the vorticity exchange across the adjacent vortex border was feeble in the screen cylinder wake, and the vorticity vectors occurred mostly along the diverging separatrices, accounting for the longitudinal slow decay. The result suggests a longer persistence of the large-scale structures in the former than that in the latter.

(4) The values of $(\overline{\overline{\tilde{\beta}\tilde{\gamma}}}/\overline{\beta\gamma})_m$ were substantially higher (28–51%) at $x^* = 10$ in the solid cylinder wake than their counterpart (4.5−22%) at $x^* = 40$ in the screen cylinder wake. The values in the former decreased rapidly from $x^* = 10{-}40$, while those in the latter increased up to $x^* = 40$ before decreasing at a much slower rate compared to the former. The observation suggests that $x^* = 40$ is the critical point where the vortices change from growing to decaying. As such, the screen cylinder wake was characterized into two regimes: vortices growth and vortex decay.

(5) The coherent motion transferred the momentum irregularly downstream and upstream of the vortex centre in the screen cylinder wake, whereas the momentum transfer occurred evenly upstream and downstream of the vortex structures in the solid cylinder wake. The incoherent motion played a predominant role in the momentum transfer in the screen cylinder wake, and the transfer took place along the separatrices overwhelmingly.

ACKNOWLEDGMENTS

A.M.A. is grateful to Universiti Teknologi MARA through BESTARI Grant No. 600-IRMI/DANA 5/3/BESTARI (P) (077/2018). The authors sincerely acknowledge the financial support from Australian Research Council (ARC) through ARC Discovery Projects DP110105171.

---

[1] R. D. Blevins, *Flow-induced Vibration*, 2nd ed. (Van Nostrand Reinhold, New York, 1990).

[2] M. M. Zdravkovich, Review and classification of various aerodynamic and hydrodynamic means for suppressing vortex shedding, J. Wind Eng. Ind. Aero. **7**, 145 (1981).

[3] M. M. Zdravkovich and J. R. Volk, Effect of shroud geometry on pressure distributed around a circular cylinder, J. Sound Vib. **20**, 451 (1972).

[4] A. M. Azmi, T. Zhou, L. Cheng, H. Wang, and L. P. Chua, On the effectiveness and mechanism of vortex-induced vibration suppression using a screen cylinder, in *Proceedings of the 22nd International Offshore and Polar Engineering Conference, International Society of Offshore and Polar Engineers, ISOPE-2012* (Rhodes, Greece, 2012), p. 586.

[5] A. M. Azmi, T. Zhou, Y. Zhou, J. Chen, and L. Cheng, The effect of a screen shroud on vortex-induced vibration of a circular cylinder and its wake characteristics, in *Proceedings of the 25th International Ocean and Polar Engineering Conference, International Society of Offshore and Polar Engineers, ISOPE-2015* (Kona, Big Island, 2015), p. 1086.

[6] F. J. Huera-Huarte, Suppression of vortex-induced vibration in low mass-damping circular cylinders using wire meshes, Mar. Struct. **55**, 200 (2017).

[7] E. M. Laws and J. L. Livesey, Flow through screens, Annu. Rev. Fluid Mech. **10**, 247 (1978).

[8] M. Miyata, Flow past 2D permeable hollow cylinder in uniform stream, in *Proceedings of the 16th International Symposium on Transport Phenomena, ISTP-16* (Prague, 2005).

[9] R. A. Antonia, T. Zhou, and G. P. Romano, Small-scale turbulence characteristics of two-dimensional bluff body wakes, J. Fluid Mech. **459**, 67 (2002).

[10] Y. Zhou and R. A. Antonia, Effect of initial conditions on vortices in a turbulent near wake, AIAA J. **32**, 1207 (1994).

[11] Z. Huang and J. F. Keffer, Development of structure within the turbulent wake of a porous body. 1. The initial formation region, J. Fluid Mech. **329**, 103 (1996).

[12] R. A. Antonia and J. Mi, Approach towards self-preservation of turbulent cylinder and screen wakes, Exp. Therm. Fluid Sci. **17**, 277 (1998).

[13] L. C. Gansel, T. A. McClimans, and D. Myrhaug, The effects of fish cages on ambient currents, J. Offshore Mech. Arct. Eng. **134**, 011303 (2012).

[14] B. Levy, H. Friedrich, J. Cater, R. Clarke, and J. Denier, The impact of twine/mesh ratio on the flow dynamics through a porous cylinder, Exp. Fluids **55**, 1829 (2014).

[15] A. M. Azmi and T. Zhou, Passive control of vortex shedding via screen shroud, IOP Conference Series, Mater. Sci. Eng. **280**, 012028 (2017).

[16] A. M. Azmi, T. Zhou, Y. Zhou, and L. Cheng, Statistical analyses of a screen cylinder wake, Fluid Dyn. Res. **49**, 015506 (2017).

[17] A. M. Azmi, Y. Lu, and T. Zhou, The formation of vortex structures in a screen cylinder wake, IOP Conference Series, Mater. Sci. Eng. **234**, 012015 (2017).

[18] P. K. Stansby, The effects of end plates on the base pressure coefficient of a circular cylinder, Aero. J. **78**, 36 (1974).

[19] A. K. M. F. Hussain and W. C. Reynolds, The mechanics of an organized wave in turbulent shear flow, J. Fluid Mech. **41**, 241 (2006).

[20] M. Matsumura and R. A. Antonia, Momentum and heat-transport in the turbulent intermediate wake of a circular-cylinder, J. Fluid Mech. **250**, 651 (1993).

[21] H. F. Wang, S. F. M. Razali, T. M. Zhou, Y. Zhou, and L. Cheng, Streamwise evolution of an inclined cylinder wake, Exp. Fluids **51**, 553 (2011).

[22] T. Zhou, Y. Zhou, M. W. Yiu, and L. P. Chua, Three-dimensional vorticity in a turbulent cylinder wake, Exp. Fluids **35**, 459 (2003).

[23] L. W. B. Browne, R. A. Antonia, and D. A. Shah, On the origin of the organised motion in the turbulent far-wake of a cylinder, Exp. Fluids **7**, 475 (1989).

[24] Y. Zhou and R. A. Antonia, Convection velocity-measurements in a cylinder wake, Exp. Fluids **13**, 63 (1992).

[25] Z. Huang, J. G. Kawall, and J. F. Keffer, Development of structure within the turbulent wake of a porous body. 2. Evolution of the three-dimensional features, J. Fluid. Mech. **329**, 117 (1996).

[26] V. Kolar, D. A. Lyn, and W. Rodi, Ensemble-averaged measurements in the turbulent near wake of two side-by-side square cylinders, J. Fluid Mech. **346**, 201 (1997).

[27] Y. Zhou and R. A. Antonia, Memory effects in a turbulent plane wake, Exp. Fluids **19**, 112 (1995).

[28] C. H. K. Williamson, Vortex dynamics in the cylinder wake, Annu. Rev. Fluid Mech. **28**, 477 (1996).

[29] A. Roshko, Structure of turbulent shear flows—New look, AIAA J. **14**, 1349 (1976).

[30] R. A. Antonia, L. W. B. Browne, D. K. Bisset, and L. Fulachier, A description of the organized motion in the turbulent far wake of a cylinder at low Reynolds number, J. Fluid Mech. **184**, 423 (1987).